# Chapter 5

# Mechanical Performance Evaluation of TPMS Scaffolds for Bone Applications

## 5.1 Introduction

Focusing on the development of lattice structures aimed at bone ingrowth, additional relevant qualities such as nutrition transport within the structure, adequate facility for vascularization, and biocompatibility of materials which permit cell adhesion are essential. These aspects were exhaustively reviewed in Chapter 2 and the involved lattice structures in this study were analysed morphologically in Chapter 4. Mechanical characteristics of structures, on the other side, influence the control of cellular processes such as gene expression, biosynthesis, cell proliferation, destruction, and division, that are all required for tissue repair. Furthermore, the mechanical characteristics of the structure should withstand the load while simultaneously providing the required biological stimulation to stimulate the cells to proliferate (Adachi et al. 2006). However, mechanical properties mismatch of the host bone to the scaffold will lead to failure in long term applications owing to the stress shielding phenomena. To address issues related, porous TPMS lattice structures found the promising candidates, since the mechanical properties of porous structures can be adjusted to match that of bone by changing its porosity, thus, other parameters will be equally tuned to obtain a mechanical property match. To this aim, this chapter focuses on, evaluation of mechanical properties at different volume fraction, the structures were already identified for this work in Section 4.1 of Chapter 4.

Further, to investigate the mechanical behaviours of the structures in an optimal time and limited computational resources, we have made some inclusion and exclusion criteria and bifurcation of the mechanical evaluation, for the lattice structures which are based on the morphological analysis performed in Chapter-4 and hypothesis drawn from the previous literature reports.

**Inclusion Criteria 1**: Lattice structures Primitive (P), Gyroid (G), Diamond (D), & I-Graph Wrapped Packages (IWP) were tested with 90% porosity: -

*(**Hypothesis:** Due to high porosity of trabecular bone a very low modulus 0.2 to 2 GPa is usually obtained. The Hypothesis that structures of high porosity are expected to give very low modulus and strength).*

**Inclusion Criteria 2**: Primitive (P), Gyroid (G), Diamond (D), & I-Graph Wrapped Packages (IWP) were tested for the porosity ranges from 50% to 80% for 10% interval.

*(**Hypothesis:** Based on high density and low porosity of cortical bone usually high modulus is reported in literature 4 to 30 GPa. The hypothesis that structures with less porosity level are expected to give high modulus and strength).*

**Exclusion Criteria**: Primitive (P), Gyroid (G), Diamond (D), & I-Graph Wrapped Packages (IWP) with porosity of 40% were excluded from mechanical property evaluation as pore sizes were exclusively out of range (shown in morphological analysis) which do not support the bone ingrowth and differentiation as reported in previous literature.

### 5.2 FEA simulations of lattice structures

#### 5.2.1 Lattice structure dimensions

The finite element analysis was performed on all lattices in ANSYS 2021R1 to predict the mechanical behavior. It is worth mentioning here that the lattice size used here was 2 × 2 × 2 mm, as studies performed in Section 3.6 on the finite number of unit cells in the lattice and finite size of structures appropriate for FEA, revealed that the size of the lattice influences the variation of numerical outcomes. In this context, selecting a higher-order lattice size does not influence mechanical characteristics, rather it will result in a larger number of output files and a higher computational cost and memory. In lower-order lattice size, higher strains can reduce

the true elastic modulus. Owing to the above-mentioned issue, we selected a 1 × 1 × 1 mm unit cell size which was uniquely patterned along the x, y, and z axes of the global Cartesian coordinate system to generate the 2 × 2 × 2 mm lattice structure. So, a total of four different structures of each having five different porosity level were used in this study.

### 5.2.2 Material Properties used

The linear and bilinear isotropic hardening material properties of porous lattices were assigned that correspond to Ti6Al4V alloy having an elastic modulus of 107 GPa and the Poisson ratio of 0.323 and detailed material properties of Ti6Al4V alloy are given below in Table 5.1. To study the elastic-plastic material behavior of all the models, the bilinear isotropic hardening (BISO) feature in the ANSYS software is used. However, TPMS realization is only possible by additive manufacturing technology, therefore we have used the material model of Ti6Al4V which is similarly used in printing through SLM method.

**Table 5.1**: Material Properties of Ti6Al4V (Yánez et al. 2018)

| Property Parameters | Values |
|---|---|
| Density | 4.405E-06 kg/mm3 |
| Elastic Modulus | 107000 MPa |
| Poisson's Ratio | 0.323 |
| Yield strength | 1098 MPa |
| Tangent Modulus | 1332 MPa |

### 5.2.3 Mesh preparation and element technology

All the scaffold models were imported into the Ansys workbench, where meshing was performed with a higher-order 3D-20-node tetrahedral/hexahedral element (SOLID186 Element). The selection of tetrahedral or hexahedral meshing is kept program controlled, in some structures where NURBS patching is not smooth which do not resemble the adjacent surface curvature (not seen by visual eye) are meshed by tetrahedral mesh.

SOLID186 are higher order elements that exhibit quadratic displacement behaviour. It has 20 nodes with 3 degrees of freedom each that correspond to nodal translation in the x, y, and z axes. The element supports plasticity which is essentially required to model the Ti6Al4V behaviour. A representative meshed model of Primitive and Gyroid model is represented in Figure 5.1. Additionally, mesh convergence study was performed to avoid variations in the finite element results. Various sizes of 0.1 mm, 0.07 mm, 0.04 mm, and 0.02 mm were adopted to eliminate the effect of mesh size on analysis. Mesh sizes of 0.04 mm and 0.02mm have shown the result independency on the mesh. The mesh element size of 0.04 mm was selected for meshing all the scaffold units to reduce discretization errors and maintain a balance between computational costs and outcome results.

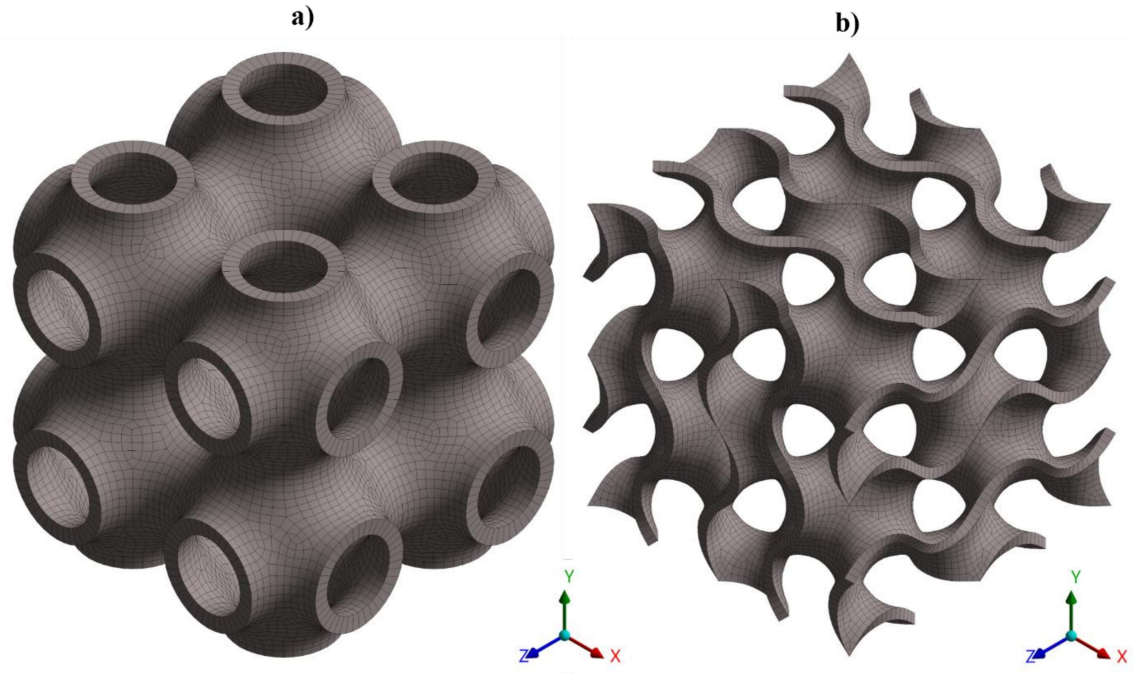


**Figure 5.1:** Representative hexahedral meshing (a) Primitive, 80% Porosity (b) Gyroid, 80% Porosity.

### 5.2.4 Loading and boundary conditions

The boundary conditions that were implemented to the model are shown in Figure 5.2. To ensure optimal load on the lattice structures, a rectangular steel plate with a thickness of 0.2 mm was developed on top surface and bottom surface of the lattices. The 3D 8-node contact elements (CONTAC174 and TARGE170) were also automatically generated by the software connecting rigid plate to lattice structures. Despite the fact that these pieces depict sliding and contact between 3D surfaces, Bonded Contact was used to describe the contacts between the surfaces of all three parts. Bonded contacts, sometimes referred to as linear contacts, connect surfaces in all directions and enable direct force transfer. Additionally, it suggests that the "small sliding" option is on, which means that only up to 20% of the contact length will be susceptible to sliding motion on the interfaces. The uniaxial vertical compressive load was applied to the top of the scaffold model, as shown in Figure 5.2. All scaffold models were compressed with the same strain rate of 5% which is equivalent to displacement loading of 0.1 mm. The displacement loading was applied with twenty sub steps to maintain the accuracy of the solution. The force reaction probe was used on the top face of bottom plate to measure the corresponding forces applied on twenty displacement sub step loading. Computations for each models took nearly about 1 hour for getting solutions up to yield maximum displacement load in a 3 GHz workstation. Since, the future scope of this work is to fabricate the mentioned scaffolds by additive manufacturing techniques, the compression test setup and loading conditions were carefully adopted according to International standard ISO 13314:2011 (Mechanical testing of metals — Ductility testing — Compression test for porous and cellular metals).

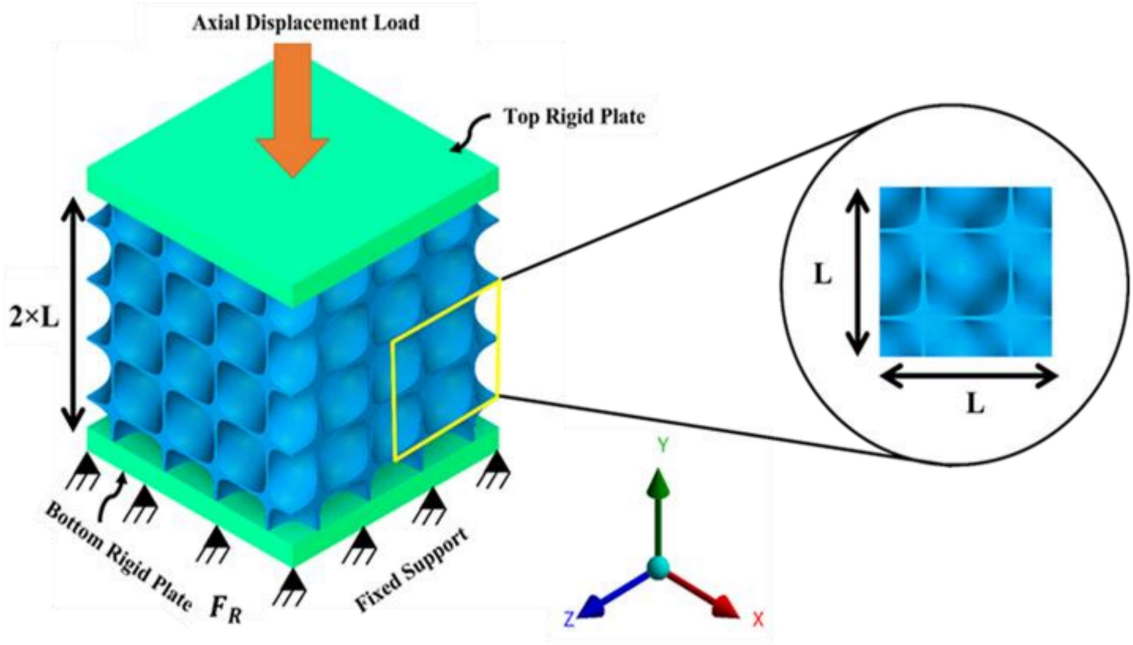


**Figure 5.2:** Illustration of loading and boundary condition of lattice structures

### 5.2.5 Measurement of mechanical properties

Stress and strains were calculated from the relation given below (Yánez et al. 2018):

$$\sigma=\frac{F_y}{A} \qquad \& \qquad \epsilon=\frac{\Delta l}{L} \tag{5.1}$$

Where σ is the stress, ϵ is the strain and $F_y$ is the force reaction of the fixed bottom rigid plate, A represents the cross-sectional area of the plate and Δl is the change in length of TPMS structures by applying displacement loading of 0.1 mm in (-Y) direction on the top plate.

Since TPMS structures are symmetric in all three Cartesian coordinates, thus, elastic modulus in each direction will be equal and defined by $E_x=E_y=E_z$.

Where, $E_x$, $E_y$, and $E_z$ are elastic modulus in X, Y, and Z coordinates. Consequently, effective elastic modulus ($E_{eff}$) was measured by fixing a trend line to linear region of stress-strain curve.

The compressive strength of every model was determined using the 0.2 % offsetting yield strength, as this is the stress where the stress-strain curve deviates by 0.2 % from the linear-elastic area for axial loading (Cain et al. 2015).

### 5.2.6 Mechanical Results and discussions for High Porosity Lattice Structures

**(Inclusion criteria 1)**

#### 5.2.6.1 Deformation behaviour of lattice structures

Figure 5.3 shows the directional deformation contours in the longitudinal direction when plastically deformed at a maximum displacement load of 0.1 mm. At the bottom of the image, a maximum corresponding force of 0.1 mm displacement force is presented. Lattice structures D, G, IWP, and P structures experience a maximum force of 194.8 N, 185 N, 183.44 N, and 123.8 N, respectively. It signifies that the D lattice structure has the maximum load-bearing capacity whereas the P lattice has the minimum. Overall, G and IWP lattices have also shown a lower range of values in comparison to the D lattice structure.

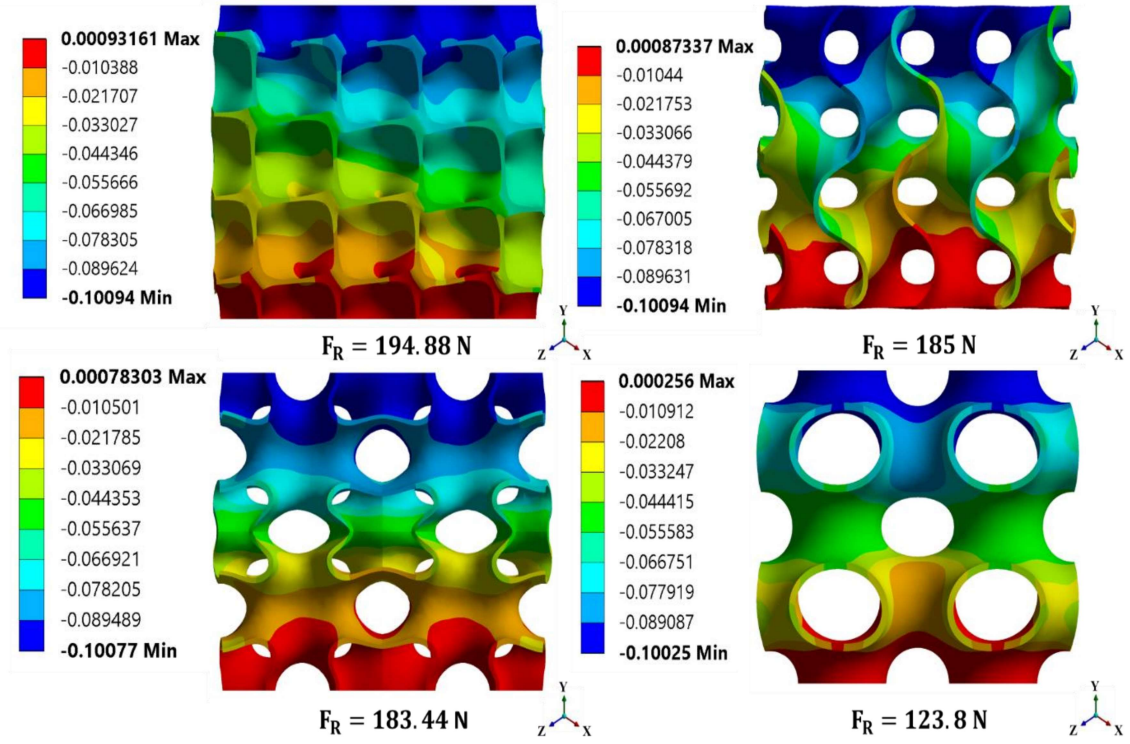


**Figure 5.3:** Illustration of Directional deformation from FEA simulation. TPMS models are Top-Left (D-Lattice), Top-Right (G-Lattice) Bottom-Left (IWP-Lattice), and Bottom-Right (P-Lattice) respectively, with identical loading conditions and material property for all lattices.

### 5.2.6.2 Stress-strain behaviour

Stress-strain curves of D, G, IWP, and P structures are shown in Figure 5.4. The stress-strain curve is split into two portions. The first represents linear elastic deformation region, while the second shows a plastically deformed plateau region. The smooth uprise plateau of all the structures predicts the ductile nature of the structures when fabricated by additive manufacturing techniques.

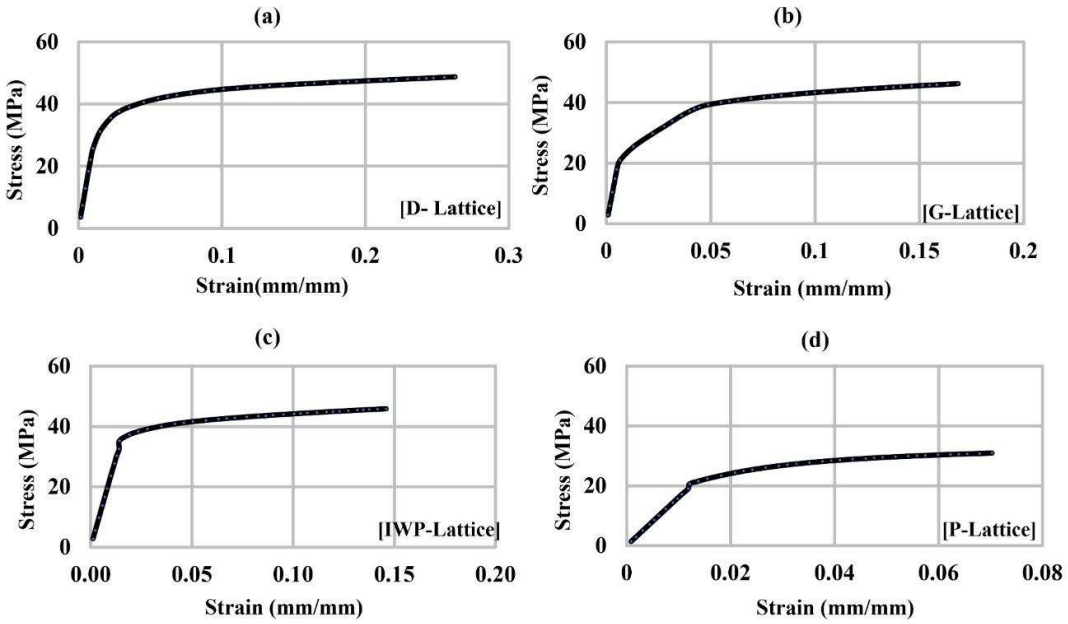


**Figure 5.4:** Compressive Stress-Strain curve of four analyzed lattice structures with 90% porosity.

### 5.2.6.3 Effective elastic modulus ($E_{eff}$)

$E_{eff}$ was calculated by fixing a trend line to linear region of compressive stress-strain curve and results are plotted in Figure 5.5 for Ti6Al4V material. It is evident that the $E_{eff}$ of Ti6Al4V is reduced from 107 GPa to a range of 1.6 – 3.5 GPa for all four structures, which has a reduction of approximately 97% as shown in Figure 5.6 and is represented under the identical porosity of 90%. G sheet possesses the highest $E_{eff}$ and P has the lowest for Ti6Al4V. The reduced range (1.6 – 3.5 GPa) depicts that these scaffolds can be used for bone application because the $E_{eff}$ of bone lies in the range of 0.05–30 GPa (Wieding et al. 2012, Li et al. 2016, Rho et al. 1997). The calculated $E_{eff}$ for all structures are listed in Table 5.2.

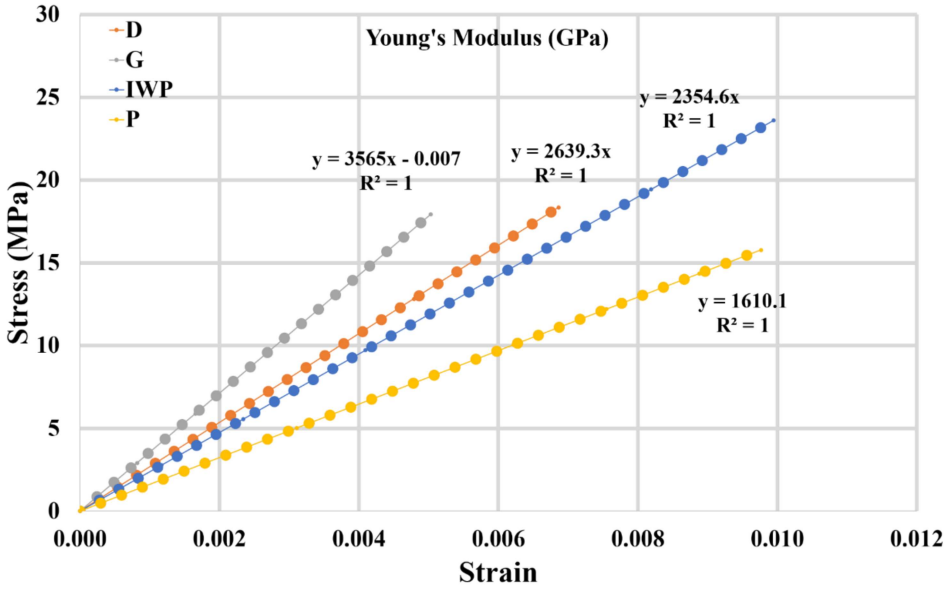


**Figure 5.5:** Demonstration of Effective Elastic Modulus ($E_{eff}$) of D, G, IWP, and P lattice drawn from linear region fit of a straight line on the compressive stress-strain curve.

**Table 5.2:** Calculated Effective Elastic Modulus ($\mathbf{E_{eff}}$) of D, G, IWP, and P.

| Lattice | D | G | IWP | P |
|---|---|---|---|---|
| **Effective Modulus (GPa)** | 2.6393 | 3.565 | 2.354 | 1.61 |

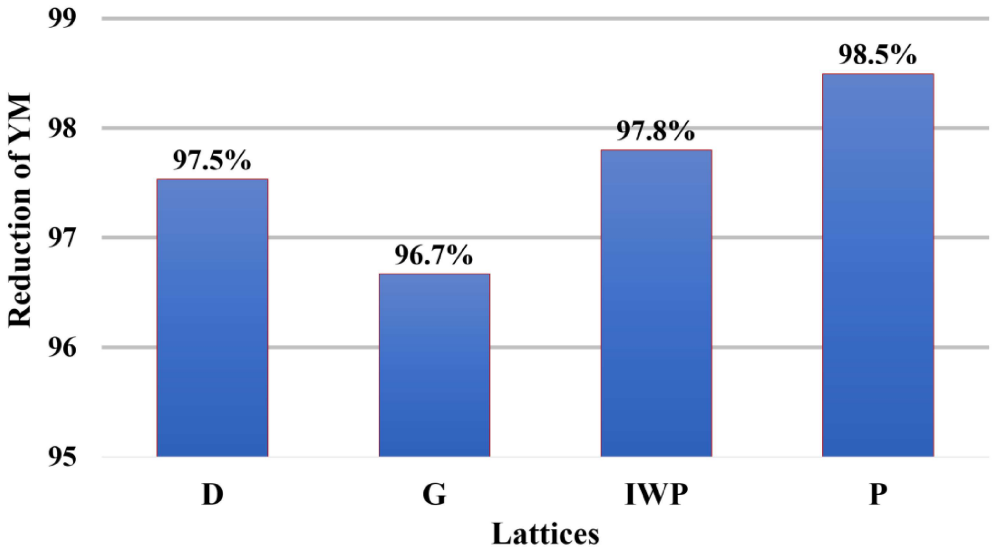


**Figure 5.6:** Reduced Elastic Modulus of solid Ti6Al4V on all four types of lattices

#### 5.2.6.4 Compressive strength

To obtain the compressive strength of all the four structures modeled with Ti6Al4V, a line parallel to the linear region of the compressive stress-strain curve was constructed but offset in a positive direction with 0.2%. Slope and intersections of this offset line with stress-strain curve were also evaluated. The compressive strength of all the structures is shown in Figure 5.7. It varies from 22 MPa to 36.8 MPa. The values from Figure 5.7 suggest that all the structures can provide strength, which can potentially emulate the human bone.

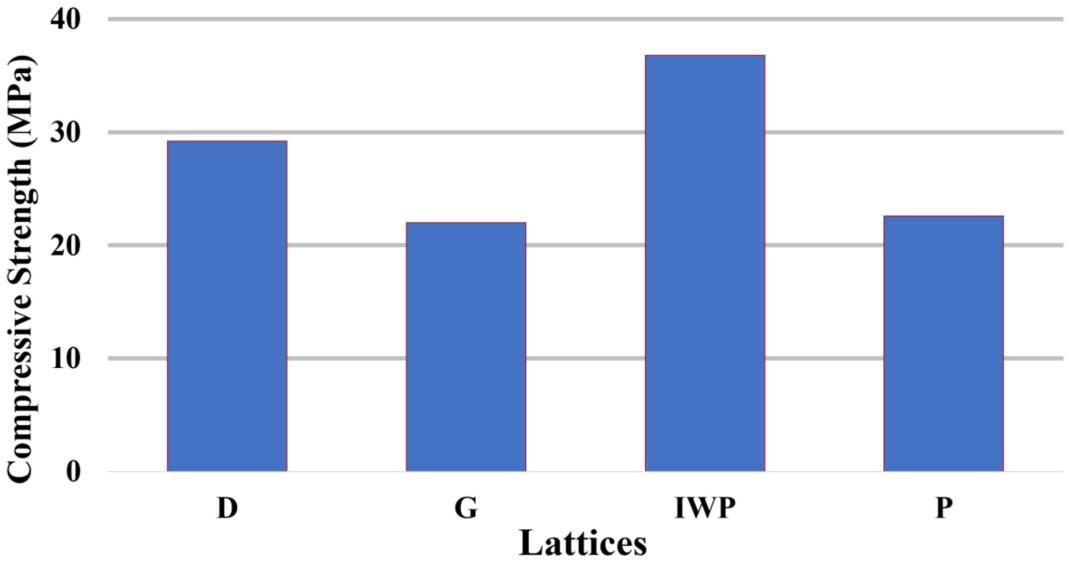


**Figure 5.7:** Compressive strength of all four types of lattices.

G and IWP structures show slightly higher strength when compared to trabecular bone and lie in the range of human bone indicating their potential application in cortical bone replacement (Morgan et al. 2018).

### 5.2.7 Mechanical Results and discussions for Lattice Structures having porosity ranging from 50% to 80%.

**(Inclusion criteria 2)**

#### 5.2.7.1 Deformation behaviour of lattice structures

To effectively visualize the changes in strain distribution on the load of 409 N which is corresponding to a strain rate 5% when plastically deformed, all four different architectures IWP, D, P and G at a particular porosity of 70 % are shown in Figure 5.8. In the IWP sheet, high strain concentration was observed in a central area surrounded by four struts both on the right and left-hand sides. Interestingly, similar patterns of strain concentration can be observed at the bottom region on those central areas and propagating towards loading direction which exhibits stretching property of structure and in the D and P strain localization occurs at the periphery of the pores. For G and P it can be noticed from strain distribution that strain were lowest at the open edges of the struts which implies that there was no force transmission at these locations. This suggests that while designing the scaffolds based on G lattice structures, these struts must be avoided. Additionally, these struts would only contribute to scaffolds with sharp edges and corners which could compromise critical safety features (Langton et al. 2012). It was also observed that the D shows strain localization on the strut diagonally. Among all four lattice structures, the IWP lattice have shown the lowest strain value whereas G have shown the highest strain value. Observing to the legends of all the structures, the values of maximum strain for D and P is almost same.

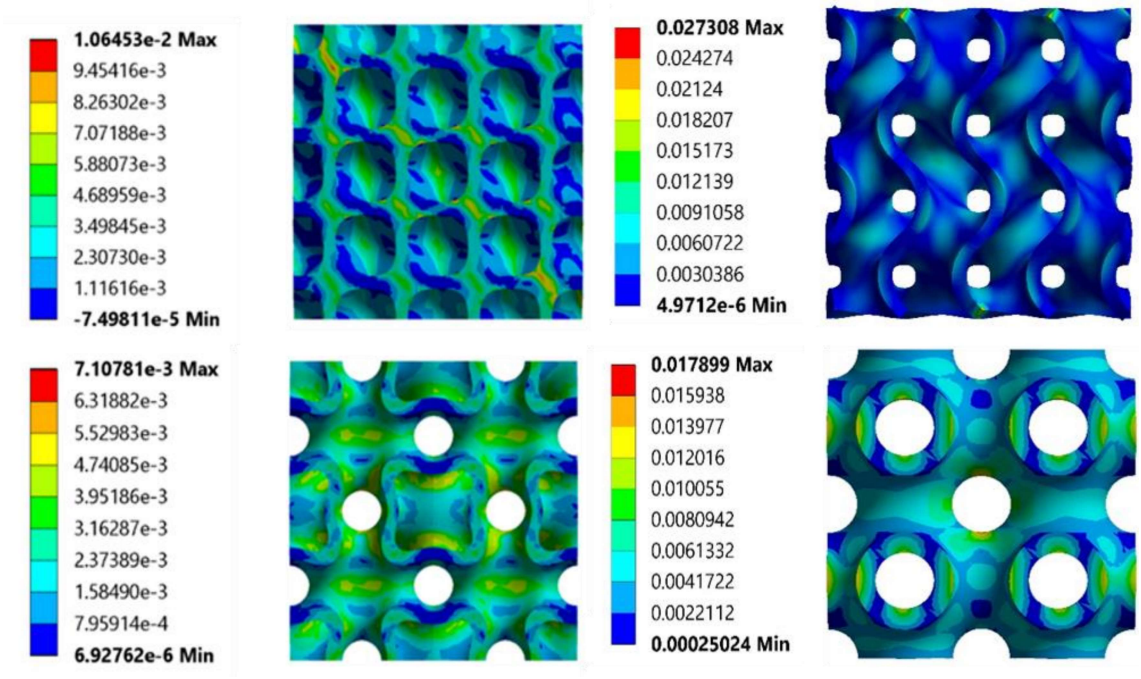


**Figure 5.8:** Illustration of Equivalent strain distribution at 409 N force of four TPMS lattice structures at porosity level of 70%.

### 5.2.7.2 Stress-strain behaviour

In the present work, a total of sixteen finite element models of four different architectures IWP sheet, IWP solid, diamond sheet, and diamond solid respectively, with varying porosities level from 50% to 80% (50%, 60%, 70%, and 80%) have been analyzed. Force reactions and strain were obtained for each model and stresses have been evaluated by dividing the force reaction of the bottom plate by the cross-section area of that plate by Equation 5.1. Typical stress-strain curves of all porous lattice structures for different porosities were plotted as shown in Figure 5.9 and have two regions i.e., a linear and a non-linear region which represent elastic as well as plastic behaviour, respectively.

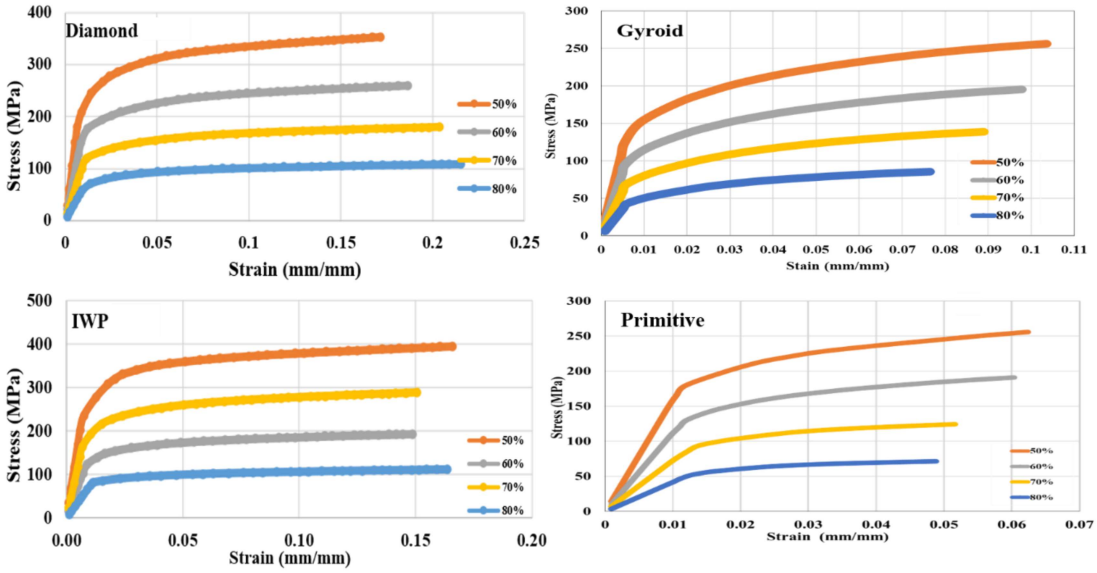


**Figure 5.9:** Compressive Stress-Strain curve of four analyzed lattice structures with varying porosity level.

### 5.2.7.3 Effective elastic modulus ($E_{eff}$)

Table 5.3 summarizes the effective Young's modulus of the IWP, D, P and G lattice structures on porosities ranging from 40% to 80%. Young's modulus decreased with increase in porosity of the lattice structures. The effective modulus for an all-lattice structures with 80% porosity have approximately 80% reduced modulus than the structures having porosity of 50%. lower than that of the P lattice with a porosity of 50%. Comparing the effective Young's modulus between all the porosity levels, P always showed the lowest modulus than other structures and IWP have shown the highest modulus while comparing to other three structures within all porosity ranges (Figure 5.10). It is noteworthy, comparing the modulus between the Diamond and Gyroid it can be observed clearly that the porosity of 60 % and 70% both the models have almost same modulus which implies that when recruiting these structures for bone applications need careful considerations of other parameters such as morphological and fluidic parameters along with biological findings.

**Table 5.3:** Calculated Effective Elastic Modulus ($E_{eff}$) of D, G, IWP, and P at different porosity level.

| Porosity (%) | Effective Elastic Modulus (GPa) | | | |
|---|---|---|---|---|
| | **IWP** | **Diamond** | **Gyroid** | **Primitive** |
| **50** | 34.24 | 28.37 | 22.77 | 16.02 |
| **60** | 23.96 | 18.08 | 16.73 | 11.24 |
| **70** | 14.4 | 11.26 | 11.62 | 7.26 |
| **80** | 7.39 | 6.42 | 7.16 | 4.21 |

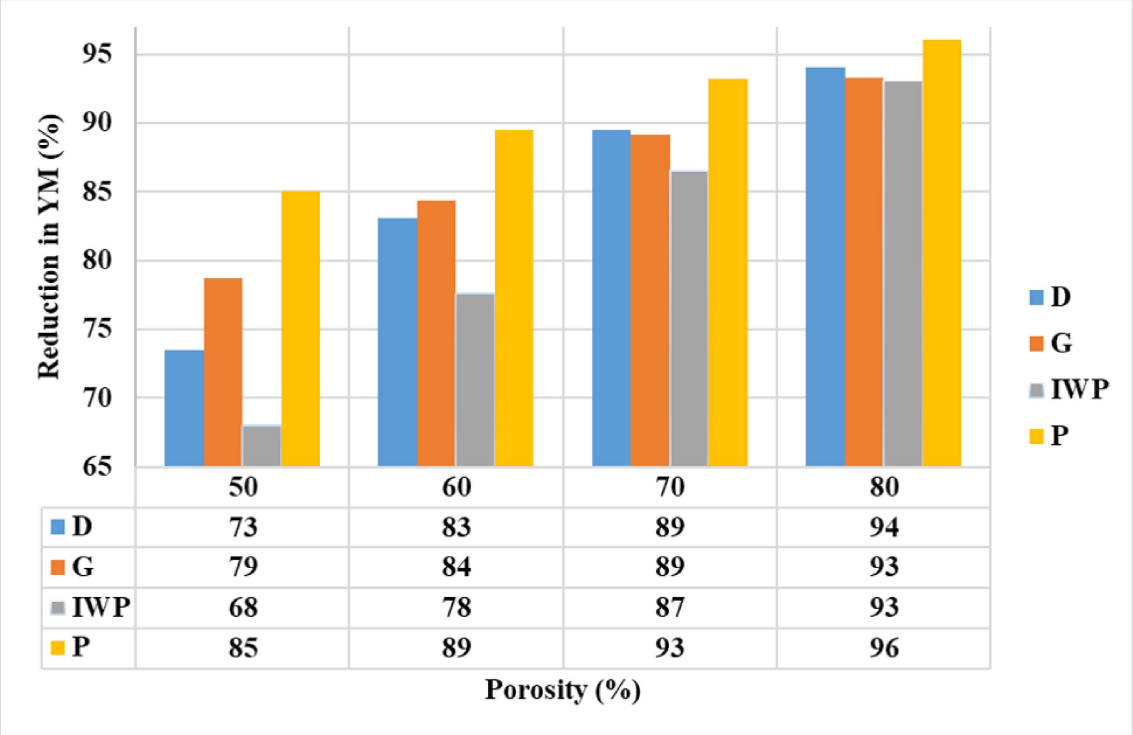


**Figure 5.10:** Reduced Young Modulus of solid Ti6Al4V on all four types of lattices for different porosity level.

On the basis of porosity level, the modulus is also varying which implies that these structures can be used as graded level of material properties as observed the bone architecture at microstructural level.

#### 5.2.7.4 Compressive strength

From Figure 5.11 it can be clearly observed that compressive characteristics for all structures having decreasing trend when porosity level increases. The compressive strength for the structures with porosity ranging from 50% to 80% with a 10% interval ranges as 258 MPa to 84 MPa for IWP, 215 MPa to 72 MPa for Diamond, 148 MPa to 48 MPa for Gyroid and 185 MPa to 56 MPa for Primitive respectively. Overall, comparing among different structures, IWP have shown the highest compressive strength whereas Gyroid have shown the lowest strength among all porosity level.

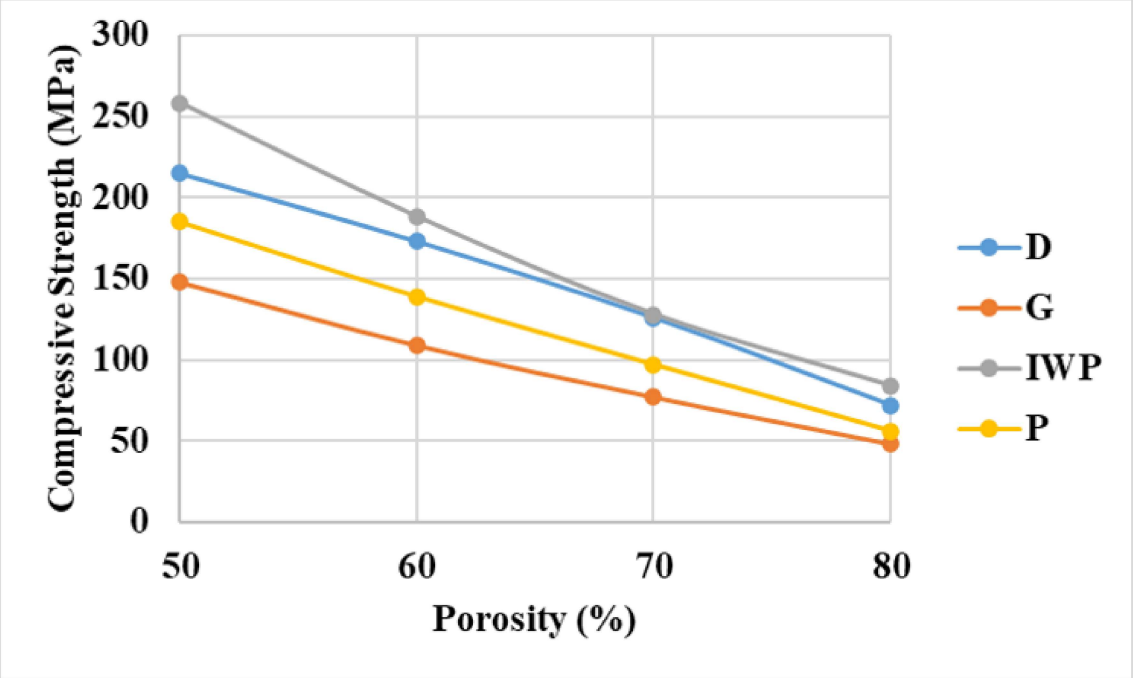


**Figure 5.11:** Compressive strength of scaffolds with varying porosity level.

### 5.3. Summary

For the numerical simulations of scaffold, It was found that porosity have the direct influence on the mechanical properties which are modulus of elasticity and compressive strength. When comparing all types of porosity, IWP showed the largest value, whereas Gyroid scaffold

showed a minimum value for the elastic modulus. Diamond and Primitive demonstrated mid-range modulus of elasticity and low strength when compared with corresponding IWP and Primitive. The computational analysis revealed that a potential porous implant can be achieved for bone applications, which can effectively reduce the modulus of the structures. When comparing these mechanical properties with bone properties, overall, Gyroid and Primitive has shown a good agreement to obey the biomechanical characteristics similar to bone. Besides, there are several limitations to using this method, which need further research. However, for making a definitive argument for the use of these findings for fabricating orthopaedic implants, there is a need for experimental testing and characterizations.

This chapter is concerned with the evaluation of mechanical properties of the developed TPMS based porous structures with different porosity ranges. The variation of properties has a direct correlation on the topology, porosity and the material used. To this end, we have tabulated the properties in Table 5.4, the mechanical properties of cortical and trabecular bone as well as other structures mechanical properties to make a direct comparison of our evaluated properties. Overall, purpose of this data is to provide a complete information at one place, which will support researchers for the basis of selection of porous structures when planning to fabricate the implants for treatment of large bone defects.

**Table 5.4:** Mechanical properties of various porous structures modelled with different materials.

| Design | Materials | Porosity (%) | Mechanical properties | | References |
|---|---|---|---|---|---|
| | | | Young Modulus (GPa) | Compressive Strength (MPa) | |
| *Cortical bone | | | 14.0 ± 9 | 109.60± 4.70 | (Guo et al. 2019) |
| *Cancellous bone | | | 0.79 ± 0.78 | 55.30 ± 8.60 | (Gu and Zheng 2010, Bobbert et al. 2017) |
| Body cantered cubic | Ti6Al4V | 53.06 ± 0.01<br>71.87 ± 0.01<br>51.90 ± 0.02 | 4.6 ± 0.4<br>1.6 ± 0.2<br>3.5 ± 0.5 | 192 ± 14<br>53 ± 4<br>86 ± 11 | (Onal et al. 2018) |
| BCCZ | Ti6Al4V | 72 | 2.20 | 31.70 ± 13.00 | (Ahmadi et al. 2014) |
| D surface | Photopolymer resin | 30 | 336.00 | 14.60 | (Yan et al. 2015) |
| | | 60 | 79.50 | 3.50 | (Yan et al. 2015) |
| I-WP surface | Photopolymer resin | Graded 40 to 60 | 234.8 | 10.00 | (Afshar et al. 2016) |
| Dodecahedron | Ti6Al4V | 62.1 | 6.30 ± 0.10 | --- | (Liu et al. 2016) |
| FBCCZ | Ti35Zr28Nb | 49.9 ± 3.2 | 1.3± 0.1 | --- | (Li et al. 2019) |

**Properties varied in various literature. This is obivious due to physiochemical variations in human populations.*

Following compression loading using a FEA programme, it was discovered that the lattice structures' local stresses were highest in BCC at the same degree of force. In contrast to BCC, BCC-Z displayed reduced local stresses. Essentially, this finding supports the weaker characteristics found in the BCC lattice structure. FCC-Z exhibited low stresses than FCC. For precise loading levels, the average FCC/FCC-Z strain value were lower than those of BCC and BCC-Z. The observed variance in strain levels despite the same loading and dimensions demonstrates the relevance of lattice structure type.